






Article

Structural and Textural Characteristics of Municipal Solid Waste Incineration Bottom Ash Subjected to Periodic Seasoning

Barbara Dutka ¹, Simona Rada ^{2,3}, Katarzyna Godyn ^{1,*}, Dumitrita Moldovan ², Ramona Ioana Chelcea ² and Maciej Tram ¹

- ¹ Strata Mechanics Research Institute, Polish Academy of Sciences, 30-059 Krakow, Poland; dutka@imgpan.pl (B.D.); maciej.tram@imgpan.pl (M.T.)
- ² Department of Physics and Chemistry, Faculty of Materials and Environmental Engineering, Technical University of Cluj-Napoca, 400114 Cluj-Napoca, Romania; simona.rada@itim-cj.ro (S.R.); dumitrita.corpodean@phys.utcluj.ro (D.M.); ramona.chelcea@phys.utcluj.ro (R.I.C.)
- ³ National Institute of Research and Development for Isotopic and Molecular Technologies, 400293 Cluj-Napoca, Romania
- * Correspondence: godyn@imgpan.pl

Abstract: The objective of this study was to determine the structural and textural description of municipal solid waste incineration (MSWI) bottom ash that was subjected to a six-month seasoning process. Bottom ash samples, with a particle size fraction of 0.063–0.1 mm, were seasoned in a closed landfill and collected for laboratory analyses at monthly intervals. The research focused on determining the structural parameters, using methods such as nuclear magnetic resonance spectroscopy (¹H NMR), X-ray diffraction (XRD), Fourier transform infrared spectroscopy (FTIR), ultraviolet-visible spectroscopy (UV-Vis), and the textural parameters, using low-pressure nitrogen adsorption (LPNA) at –196.15 °C. The analyses of the porous structure of the bottom ash samples revealed differences in texture of ASH 1 to ASH 6, specifically in the pore volume (micro- and mesopores), specific surface area, and pore size distribution. Changes in the structural and porous characteristics of the samples were attributed to the duration of the seasoning process. The results of the structural analysis of the bottom ash suggest its application in the concrete industry, potentially enhancing the long-term mechanical strength of concrete. The results of the textural analysis indicate the possible use of MSWI bottom ash in environmental applications, as the internal surface area could be further developed.

Keywords: MSWI bottom ash; structure; texture; low-pressure nitrogen adsorption; surface area; pore volume; ¹H NMR; XRD; FTIR; UV-Vis



check for updates

Citation: Dutka, B.; Rada, S.; Godyn, K.; Moldovan, D.; Chelcea, R.I.; Tram, M. Structural and Textural Characteristics of Municipal Solid Waste Incineration Bottom Ash Subjected to Periodic Seasoning. *Sustainability* **2024**, *16*, 9597. <https://doi.org/10.3390/su16219597>

Academic Editor: Antonio Zuorro

Received: 13 October 2024

Revised: 30 October 2024

Accepted: 1 November 2024

Published: 4 November 2024



Copyright: © 2024 by the authors. Licensee MDPI, Basel, Switzerland. This article is an open access article distributed under the terms and conditions of the Creative Commons Attribution (CC BY) license (<https://creativecommons.org/licenses/by/4.0/>).

1. Introduction

The generation of municipal solid waste is a global issue today. Thermal waste treatment is a key method for reducing the volume of post-consumer residues. This process involves high-temperature conversion in the municipal waste incineration plants, which are widespread across Europe. In Poland, there are currently eight incineration plants, primarily treating unsorted municipal waste and residues from municipal waste processing [1]. The incineration process results in MSWI bottom ash (known also as bottom ash and slag or BA), accounting for about 30% of the input mass; fly ash, accounting for about 4%; exhaust gases; and energy production [2,3]. From 1 ton of municipal solid waste, around 300 kg of solid residue is produced, which, after proper seasoning and valorization, could be utilized as a raw material for new products [4]. Incineration contributes to minimizing the space required for conventional landfills.

According to regulations, bottom ash, classified as non-hazardous waste with the 19 01 12 code, has the potential to be developed into new products [5]. Developing a methodology for utilizing this waste as a new product aligns with the goals of a circular economy, following European Union policies. The 12th of the Sustainable Development

Goals (SDGs) emphasizes the importance of responsible consumption and production, where recycling post-process residues plays a vital role. Effective waste management solutions are essential for the recycling process [6]. The possibility of utilizing bottom ash and slag is crucial for environmental protection [7,8]. Such strategies preserve natural resources, reduce waste, and release the areas that were previously allocated for landfills [9].

The chemical and mineral composition of bottom ash from municipal waste incineration resembles that of cement, which is widely used in construction materials. The particle size distribution of bottom ash is similar to aggregates that are commonly used in concrete (EN 12620, 2002) [10].

In some countries, bottom ash is used for road sub-bases or considered as a raw material for various building products [11,12]. Bottom ash, alongside fly ash, has potential applications in cement and concrete production [13–17]. Therefore, it is essential to understand the structure and texture of bottom ash and its fractions (from slag to ash). Studies have shown that fly ash has a very low specific surface area, of just a few m^2/g . However, transforming fly ash into a zeolitic structure significantly increases its micropore space and CO_2 adsorption capacity [18]. The similar oxide composition between bottom ash and fly ash suggests a potential for enhancing internal surface area and sorption capacities, which are useful for capturing pollutants like CO_2 [19].

The chemical composition of bottom ash, comparable to that of cement [20], includes the major components: CaO (about 68%), SiO_2 (about 14%), Fe_2O_3 (about 5%), and Al_2O_3 (about 4.5%). For any potential use in construction, particle size and fragmentation are important considerations [20]. Bottom ash could be used in two ways: as a cement substitute or as filler aggregate. Cement applications require finely ground material, yielding a highly durable product. Fly ash and coal bottom ash have successfully replaced Portland cement due to their small particle size [21,22]. Using bottom ash as an aggregate seems more feasible and straightforward.

Macroscopic observations showed that bottom ash has a high affinity for water. When it dries, it absorbs moisture from the air, causing the finer particles to adhere to container walls or solidify in closed containers. This property may benefit cement mortar binding. Porosity, pore structure, and pore size distribution significantly impact the physical properties, like strength, deformability, and permeability, of general-purpose building materials [6]. Furthermore, the texture of bottom ash influences water demand and flowability in fresh mortar [10]. The average pore width of bottom ash (14.2 nm) allows heavy metals to be encapsulated within the matrix, reducing leachability [23]. It was found that bottom ash has about 3.66 times the adsorption capacity of fly ash and 2.04 times that of clay.

This article aims to demonstrate the potential use of MSWI bottom ash by investigating its structural and textural properties. Understanding these properties is crucial, as it could transform bottom ash from an environmental and economic issue into a profitable product. In the future, MSWI bottom ash could become a valuable resource in new material formulations, similar to construction and demolition waste. Chemical synthesis at ambient or elevated temperatures could create zeolitic adsorbents that are tailored for specific applications. Zeolite modification requires a mineral feedstock with a favorable Si/Al ratio, such as fly ash [24] or coal ash [25]. Finely powdered bottom ash material could be treated with sodium or potassium hydroxide, showing a similar effectiveness as has been demonstrated with fly ash. A key advantage of working with the bottom ash studied here is its classification as non-hazardous, making its products environmentally neutral. Understanding the structure and texture of bottom ash is critical for developing prospective applications.

This research involved monthly sampling from a landfill to analyze changes in the structural and textural parameters of bottom ash over a six-month period.

2. Materials and Methods

2.1. MSWI Bottom Ash

The waste material used in the study was obtained from one of the Polish municipal waste incineration plants. It consisted of slag and bottom ash (referred to as bottom ash or BA) that was produced during the thermal conversion of the municipal solid waste. MSWI bottom ash, designed as SP4, was transported to our facility and then spread out on a tarp in an closed warehouse, referred to hereafter as the landfill. At the landfill, the mineral waste could naturally undergo the seasoning process.

2.2. Samples

Six samples of bottom ash were collected from a closed landfill, each at one-month intervals from the previous sampling. The collected samples were sequentially numbered from SP4.1 to SP4.6 (see Table 1). The waste material from each collection was delivered to the laboratory and dried at temperature of 105 °C. The first step of the samples' preparation was to separate the SP4 material into several granulometric fractions, without any milling, to perform a sieve analysis. Oxide composition analyses of the SP4 bottom ash were carried out in an accredited chemical laboratory using the X-ray fluorescence method (XRF). For the structural and textural studies, the bottom ash samples with a sand fraction of 0.063–0.1 mm were selected and labeled according to the information provided in Table 1.

Table 1. Bottom ash samples prepared for studies.

Sampling Number	Date of Collection from the Landfill	Seasoning Time (Week)	Collected Bottom Ash Designation	Mass of Collected Bottom Ash (g)	Sample Designation (0.063–0.1 mm)
1	14 November 2022	6	SP4.1	2975.9	ASH 1
2	19 December 2023	11	SP4.2	1447.0	ASH 2
3	20 January 2023	16	SP4.3	1345.8	ASH 3
4	21 February 2023	21	SP4.4	1905.2	ASH 4
5	17 March 2023	26	SP4.5	1387.1	ASH 5
6	21 April 2023	31	SP4.6	1641.3	ASH 6

The research aimed to observe changes in the structural and textural parameters of bottom ash over a six-month period. The sample designed as ASH 1 was approximately 6 weeks old when it was removed from the incineration plant furnace. Firstly, ASH 1 was seasoned for 5 weeks at the incineration plant and, secondly, for around 1 week in a closed landfill. The subsequent bottom ash samples, ASH 2, ASH 3, ASH 4, ASH 5, and ASH 6, were collected monthly for further testing.

2.3. Structural Characterization

Laboratory tests to determine the structural parameters of seasoned bottom ash involved techniques such as nuclear magnetic resonance spectroscopy (¹H NMR), X-ray diffraction (XRD), Fourier transform infrared spectroscopy (FTIR), and ultraviolet-visible spectroscopy (UV-Vis).

2.3.1. NMR

The NMR measurements were performed with the low-field NMR Bruker Minispec spectrometer (Bruker Optik GmbH, Ettlingen, Germany) at the proton frequency of 19.672 MHz. The transverse relaxation time (T₂) measurements were performed using a CPMG (Carr–Purcell–Meiboom–Gill) pulse sequence [26–29], with a total number of 2000 echoes. To enhance the signal-to-noise ratio, the number of scans was set at 1024, the recycle delay was set 0.5 s, the primary pulse at 9.3 μs, the receiver gain at 96 dB, and the

echo time (TE) was 0.07 ms. The acquired CPMG decay curves were analyzed using a fast Laplace inversion algorithm [26–29].

2.3.2. XRD

The mineral composition of the bottom ash samples was analyzed using the X-ray diffraction (XRD) method. The ash samples were characterized with a X-ray diffraction using a Rigaku diffractometer (Rigaku Corporation, Tokyo, Japan), with a Cu-K α radiation wavelength of $\lambda = 1.54 \text{ \AA}$. equipped with a high-energy and high-resolution 2D semiconductor detector. The resulting diffractograms were supplemented with a microscopic evaluation of thin sections in transmitted light.

2.3.3. FTIR

One of the main methods for the identification of varied structural units from substances is infrared spectroscopy [30]. The Fourier transform infrared (FT-IR) spectra were performed with a JASCO FTIR 6200 spectrometer (JASCO, Tokyo, Japan) and were recorded in the 400–4000 cm^{-1} range, using the standard KBr pellet disc technique [31,32].

2.3.4. UV-Vis

UV-visible absorption spectra of the powdered bottom ash samples were recorded at room temperature in the 250–900 nm range using a UV-vis spectrometer (Perkin-Elmer Corporation, Waltham, MA, USA) that was equipped with an integrating sphere. These measurements were made on bottom ash powder, dispersed in KBr pellets. The validity of the band position was $\pm 2 \text{ nm}$.

2.4. Textural Characterization

Textural parameters were determined with the adsorption method. The porous texture characterization of the seasoned bottom ash was performed using the volumetric gas physisorption technique on the ASAP 2020 analyzer from Micromeritics Instrument Corporation, Norcross, GA, USA (Figure 1). Low-pressure nitrogen adsorption and desorption isotherms were measured at a temperature of 77 K ($-196.15 \text{ }^\circ\text{C}$) for bottom ash samples weighing approximately 2.8 g. Measurements were conducted over a relative nitrogen pressure range (p/p_0) from 0 to 1, where p_0 is the saturated vapor pressure of pure nitrogen at the measurement temperature, and p is the equilibrium pressure.



Figure 1. ASAP 2020 specific surface area and porosity analyzer.

Samples of MSWI bottom ash with a granulometric fraction of 0.063–0.1 mm (see Figure 2) were subjected to nitrogen adsorption after degassing in the preparation port of the ASAP 2020 analyzer. This was done under controlled conditions at 80 °C for 12 h, achieving a pressure of approximately 10^{-5} mbar. During sorption measurements, the amount of adsorbed gas per unit mass of the sample, expressed in cm^3 STP/g, was recorded as a function of the relative equilibrium pressure, p/p_0 . Nitrogen adsorption over the full range of relative pressures allowed for the characterization of the porous structure of the MSWI bottom ash, from the microporosity range at low p/p_0 values to the mesoporosity range. In the latter, based on the phenomenon of capillary condensation at a p/p_0 close to 1, the gaseous adsorbate transitions into the liquid state. The quantity of nitrogen adsorbed at the measurement temperature was determined at $p/p_0 = 0.98$.

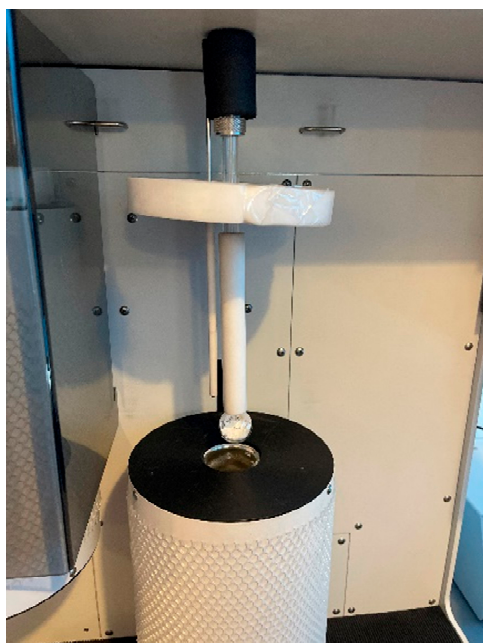


Figure 2. Sample in a Teflon-collar thermocouple with a liquid nitrogen dewar.

The textural characteristics of the six MSWI bottom ash samples were based on the parameters determined from the nitrogen adsorption isotherms. The porous texture parameters of the samples were identified, particularly the specific surface area, according to the Brunauer–Emmett–Teller (BET) theory of multilayer adsorption, total pore volume, and pore size distribution. The micropore volume and area were estimated using the t-plot method, and the Harkins and Jura equation was applied for a thickness range from 0.35 nm to 0.50 nm. The average pore size and distributions were determined using the Barrett–Joyner–Halenda (BJH) model.

2.5. Adsorption Models

2.5.1. Surface Area

The specific surface area of the bottom ash samples (in m^2/g) was determined, including the external surface (S_{ext}) and the internal surface (S_{int}). The external surface, which is inversely proportional to the grain size, corresponds to the geometric surface of porous grains relative to the adsorbent mass. The internal surface consists of the walls of the open pores within the material. A higher specific surface area corresponds to smaller pore radii.

The specific surface area of the tested bottom ash samples was determined using the Brunauer–Emmett–Teller (BET) theory of multilayer adsorption in the relative pressure range $0.05 < p/p_0 < 0.30$ [33]. As the pressure p approaches p_0 , adsorption increases, becoming multilayered, which leads to an increase in the thickness of the adsorbed layer. At $p = p_0$, the capillary condensation of the adsorbate occurs in the pores of the adsorbent,

and the isotherm passes through an inflection point. The BET adsorption isotherm model predicts the application of the Langmuir equation, which describes the coverage of the adsorbent surface with a monolayer of gas molecules to each adsorbed layer [33]. The BET multilayer adsorption isotherm equation is often presented in its linear form:

$$\frac{\frac{p}{p_0}}{a\left(1 - \frac{p}{p_0}\right)} = \frac{1}{a_m C} + \frac{C - 1}{a_m C} \frac{p}{p_0} \quad (1)$$

where a (mol/g) is the amount of adsorbed gas, a_m (mol/g) is the amount of gas required to completely cover the adsorbent surface with a monolayer of adsorbate molecules, p (Pa) represents the equilibrium pressure of the adsorbate, p_0 (Pa) is the saturation vapor pressure at the measurement temperature, and C (–) is a constant that is dependent on adsorption energy and temperature.

The amount of nitrogen needed to cover the adsorbent surface with a monolayer (a_m value) was determined from the BET surface area plot, which involves plotting the relative pressure (p/p_0) against $(p/p_0)/[a(1 - p/p_0)]$. From this plot, the slope (in g/cm³ STP); the Y-intercept (in g/cm³ STP); the constant, C (–); and the monolayer capacity, a_m (in cm³/g STP); were determined graphically. By using the molecular cross-sectional area of a nitrogen molecule, σ_m , the obtained monolayer capacity, a_m , was converted into S_{BET} , the specific surface area of the bottom ash. The following equation was used:

$$S_{BET} = a_m \sigma_m N_A \quad (2)$$

where a_m is the monolayer capacity, σ_m is the section area of adsorbate molecule in the monomolecular layer, and N_A is Avogadro number.

In calculating the areas, a value of 0.154 nm²/molecule was taken as the standard for nitrogen adsorbed at –196.15 °C [34].

The specific surface area was also measured, based on the single point BET theory, which requires determining the amount of adsorbed nitrogen at a relative pressure, $p/p_0 = 0.30$. The S_{sBET} , the specific surface area, was calculated using the following equation:

$$S_{sBET} = \frac{a_m \cdot N_A \cdot \sigma_m}{m \cdot 22,400} \quad (3)$$

where a_m is the monolayer capacity; σ_m is the cross-sectional area of one adsorbate molecule, nm²; m is the mass of the bottom ash sample, g; 22,400 is the volume occupied by one mole of the adsorbate under STP conditions, cm³; and N_A is the Avogadro number.

A standard multilayer thickness curve was constructed using the following thickness equation:

$$t = \left[\frac{13.99}{\left(0.034 - \log\left(\frac{p}{p_0}\right)\right)} \right]^{0.5} \quad (4)$$

By creating a t-plot that plotted the quantity adsorbed against the statistical thickness of the layer, it was possible to determine the external surface area of the bottom ash samples.

2.5.2. Pore Volume

The total pore volume, V_p (in cm³ per gram of the sample), was determined from the volume of adsorbed nitrogen at a relative pressure of $p/p_0 = 0.98$. The pore diameter, D_p , was calculated using the following formula:

$$D_p = 4V_p/S_{BET} \quad (5)$$

2.5.3. Micropores and Mesopores

According to the International Union of Pure and Applied Chemistry (IUPAC), pores are classified into three main groups, based on size. Smaller than 2 nm—micropores; between 2 nm and 50 nm—mesopores; and larger than 50 nm—macropores [35].

The pore size distribution of the bottom ash samples was determined from the adsorption branch of the isotherm, as it closely represents the true distribution [35]. These parameters were estimated using models that analyze capillary condensation. In the relative pressure range of $0.4 < p/p_0 < 0.98$, capillary condensation occurs in mesopores, and as the gas pressure increases, the adsorbate layer thickens on the pore walls until the pores are completely filled with liquid adsorbate. The total pore volume and pore size distribution were determined assuming a cylindrical pore model using the Kelvin equation:

$$\ln\left(\frac{p}{p_0}\right) = -\left(\frac{2\sigma V_m \cos\theta}{RT r_m}\right) \quad (6)$$

where σ (J/m²) is surface tension of liquid nitrogen, V_m (m³/mol) is the molar volume of the adsorbate, R (J/mol·K⁻¹) is the gas constant, T (K) is the absolute temperature, and r_m (m) is the radius of meniscus curvature.

The determination of pore size distributions for the bottom ash samples was carried out using the Barrett–Joyner–Halenda (BJH) method, which accurately describes the mesopore range from 2 to 50 nm and is also used for describing smaller pores with dimensions below 2 nm (micropores). The Halsey equation for the statistical thickness of the adsorbate layer with the Faas correction was applied in determining the mentioned parameters.

3. Results and Discussion

3.1. SP4 Bottom Ash

The oxide composition of seasoned bottom ash, obtained from the XRF method, is presented in Table 2.

Table 2. Oxide composition of SP4 bottom ash.

Concentration of component % (m/m)	CaO	SiO ₂	Fe ₂ O ₃	Al ₂ O ₃	SO ₃	TiO ₂	ZnO	Na ₂ O
	66.65–69.01	12.44–14.77	4.55–5.84	4.02–4.78	1.68–2.53	1.25–1.55	0.75–0.94	0.79–0.89
	P ₂ O ₅	Cl	K ₂ O	MgO	CuO	MnO	PbO	ZrO ₂
	0.73–0.86	0.71–1.26	0.70–0.74	0.60–0.88	0.29–0.51	0.12–0.16	0.06–0.10	0.03–0.04

As it may be seen from Table 2, the composition of the SP4 bottom ash showed a predominant presence of calcium oxide (CaO), followed by silicon dioxide (SiO₂), iron oxide (Fe₂O₃), and aluminum oxide (Al₂O₃). The significant CaO content suggests the potential for a carbonation process, leading to the formation of calcite from hydrated free lime [36]. The bottom ash also contained oxides of less common elements, such as TiO₂ and ZrO₂, in trace amounts.

Figure 3 shows the particle size distributions of the SP4 bottom ash that had been seasoned for periods ranging from one month to over six months in the closed landfill. As may be observed from Figure 3, the curves representing the grain size distributions of the bottom ash samples are similar over the analyzed period. Despite different seasoning durations, the distributions do not follow a specific trend. Approximately 20% of the tested samples consisted of particles that were <0.063 mm; about 5 to 10% of the composition consisted of particles sized between 0.063 mm and 0.1 mm; while 75 to 85% of the samples consisted of particles in the 1.0 mm to 10.0 mm size range.

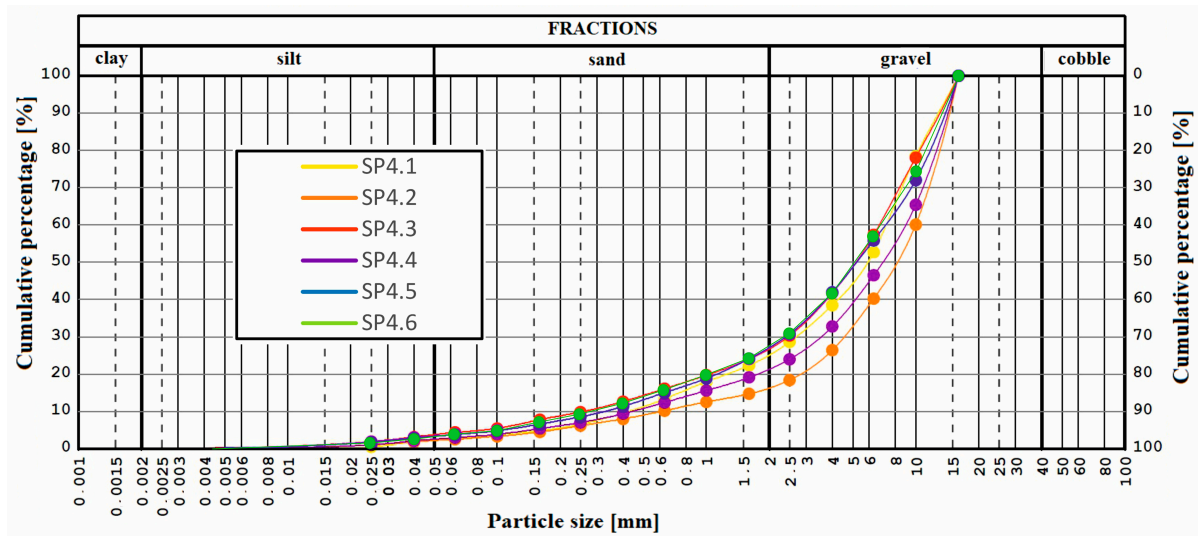


Figure 3. Particle size distributions of SP4 bottom ash seasoned for a period of one to six months.

3.2. Structural Characteristics

3.2.1. NMR Data

The CPMG decay curves were recorded for six samples: ASH 1, ASH 2, ASH 3, ASH 4, ASH 5, and ASH 6 (see Figure 4A). To allow for a direct comparison, the CPMG echo train plots were normalized to the first point, and the normalized distribution of the transvers relaxation times were obtained and plotted together in Figure 4B. These are characterized by a number of four peaks extended on a range from 10 μ s to 100 ms, indicating the presence of various components with different dynamics (at the molecular level), from the most rigid, ^1H (associated with peaks characterized by T_2 values of the order of tenths of microseconds), to the most mobile, ^1H (associated with peaks characterized by T_2 values of the order of tenths of milliseconds). These components can be associated with ^1H from bound water and with those from small, medium, and large pores. The difference in the dynamics of the samples can be observed, especially for the ASH 5 and ASH 6 samples, which are more rigid. All of the samples have a predominant component between the 7.16×10^{-5} – 1×10^{-4} ms values, indicating the pore rigidity and the low amount of water in the pores. The dynamics of the first two, ASH 1 and ASH 2, are similar, but the amplitudes of the pores are smaller in ASH 2. Instead, the ASH 3 sample has only three components, which indicates the migration of the peak from the 1.53×10^{-4} ms value to the predominant peak of the T_2 -distribution. This migration demonstrates unfinished activity at the micropores level of ASH 3, associated with CaO components. In samples ASH 4, ASH 5, and ASH 6, the main peak is the one that is well resolved and has an amplitude comparable to the sample ASH 2; the peaks from 10^{-3} have a relatively small integral area, almost null, which can lead to the conclusion that the samples are drying.

3.2.2. XRD Analysis

Figure 5 shows X-ray diffractograms of the studied samples. All of the samples contain the crystal phases of CaCO_3 with a rhombohedral structure and SiO_2 with a hexagonal structure. SiO_2 occurs in the form of quartz grains, which were observed in large numbers using an optical microscope (Figure 6). The crystal phase CaCO_3 , which has been identified as calcite, also appears in large numbers. Microscopic analyzes also confirmed the presence of other mineral phases, such as feldspar, melilite, apatite, anhydrite, gypsum, and wollastonite [37], but they are rare and are, therefore, not visible in the diffractograms.

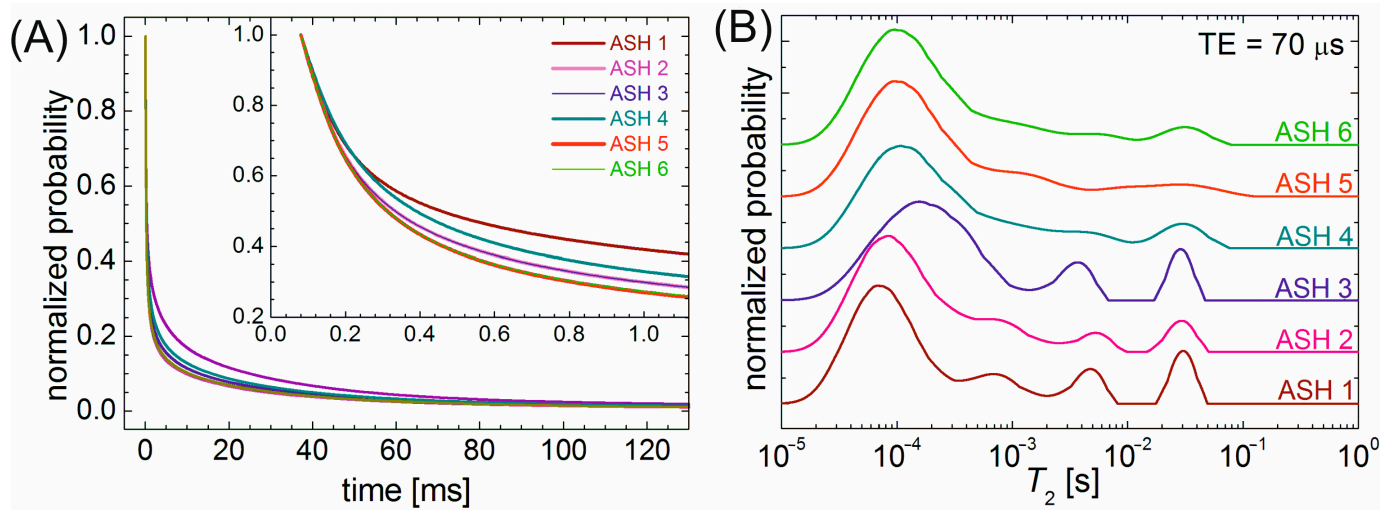


Figure 4. (A) CPMG decay for all samples and (B) T_2 distribution curves measured by ^1H NMR relaxometry for ASH 1 to ASH 6.

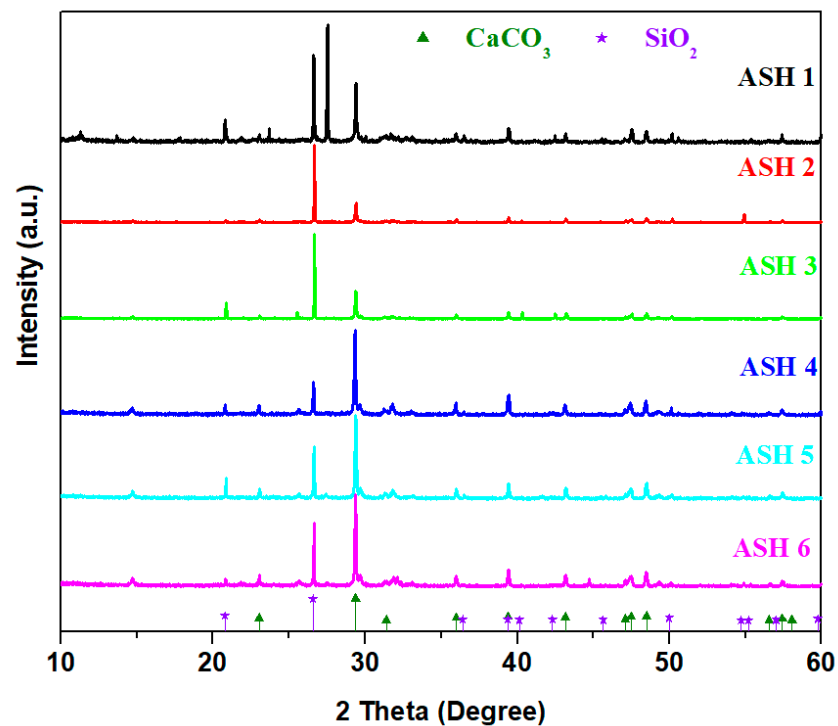


Figure 5. XRD patterns of the studied bottom ash samples.

For the sample ASH 1, the presence of an intense diffraction peak, which is centered at 27.42° and corresponds to the FeSO_4 crystalline phase, is highlighted. This peak disappears below the detection limit of the diffractometer for the other samples. The intensity of the main diffraction peak attributed to the crystalline phase of calcium carbonate decreases for samples ASH 4 and ASH 5, indicating a decrease in the content of this phase in the samples. There is a significant metallic admixture in the analyzed samples, probably the crystalline phase of iron [37]. The intensity of the diffraction peak that is located at 27.54° and corresponds to the crystalline phase of silicon dioxide reaches minimum values for samples ASH 2 and ASH 3. The presence of the two crystalline phases, SiO_2 and CaCO_3 , in the ash suggests the potential for applications in the concrete industry, and CaCO_3 provides long-term mechanical strength to concrete.

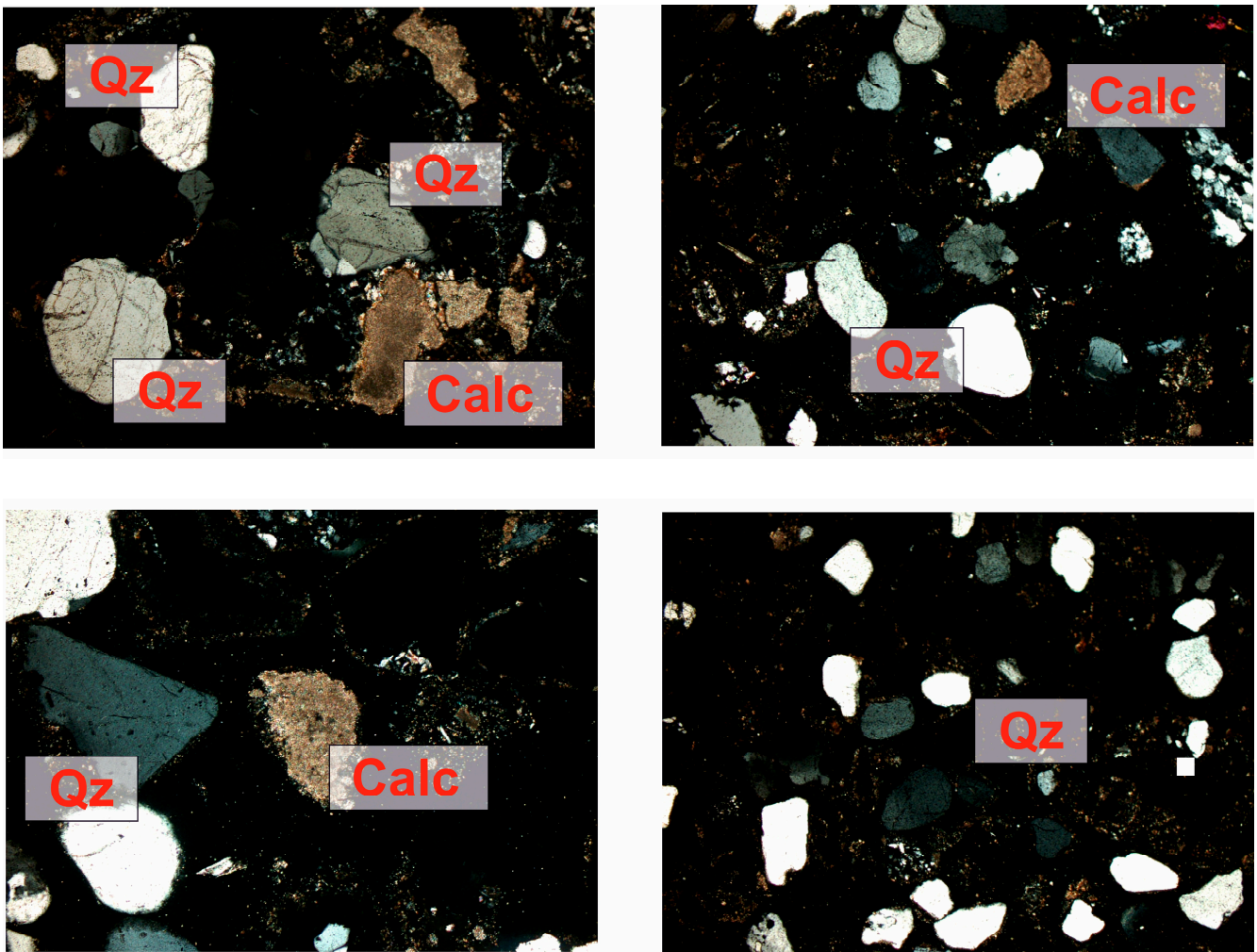


Figure 6. Minerals found in slags and ashes. Qz—quartz; calc—calcite. Thin section, 1P, 50–100 \times , transmitted light.

3.2.3. FTIR Analysis

The FTIR spectra of the ASH 1 to ASH 6 samples are shown in Figure 7. All of the spectra exhibit several peaks, indicating the presence of various functional groups in the bottom ash samples. The IR spectra present characteristic peaks at various wavenumbers that can be correlated with the stretching vibrations of the chemical bonds or the bending vibrations of the angles that are specific to varied structural units. The first range of IR bands, located between 400 and 580 cm^{-1} , come from Si-O-Si deformation vibrations and metal-oxygen stretching vibrations. The lower intensity IR bands, centered at 600 and 1100 cm^{-1} , correspond to S-O elongation vibrations in sulfate units [31]. The intensity of the IR bands in this region appears to be slightly modified for sample ASH 1 compared to the other samples. This change can be attributed to the presence of the FeSO_4 crystalline phase, which contained sulfate units. The IR band at 720 cm^{-1} is attributed to elongation vibrations of the Ca-O bond. The IR bands centered at about 875 and 1450 cm^{-1} correspond to deformation and elongation vibrations, respectively, in the carbonate structural units [31]. The region of IR bands lying between 900 and 1250 cm^{-1} is attributed to different vibrations in silicate units [31]. The prominent FT-IR band, centered at about $\sim 3450 \text{ cm}^{-1}$, is assigned to the O-H asymmetric stretching vibrations from adsorbed water molecules on the surface of the sample [28]. This region typically corresponds to O-H stretching vibrations, often seen in hydroxyl groups and water. ASH 1, ASH 4, and ASH 6 show that the intensity of this band is stronger, indicating the presence of water and/or hydroxyl units in the samples.

Then, ASH 2, ASH 3, and ASH 5 show less pronounced bands in this region, suggesting lower hydroxyl or water content in the samples.

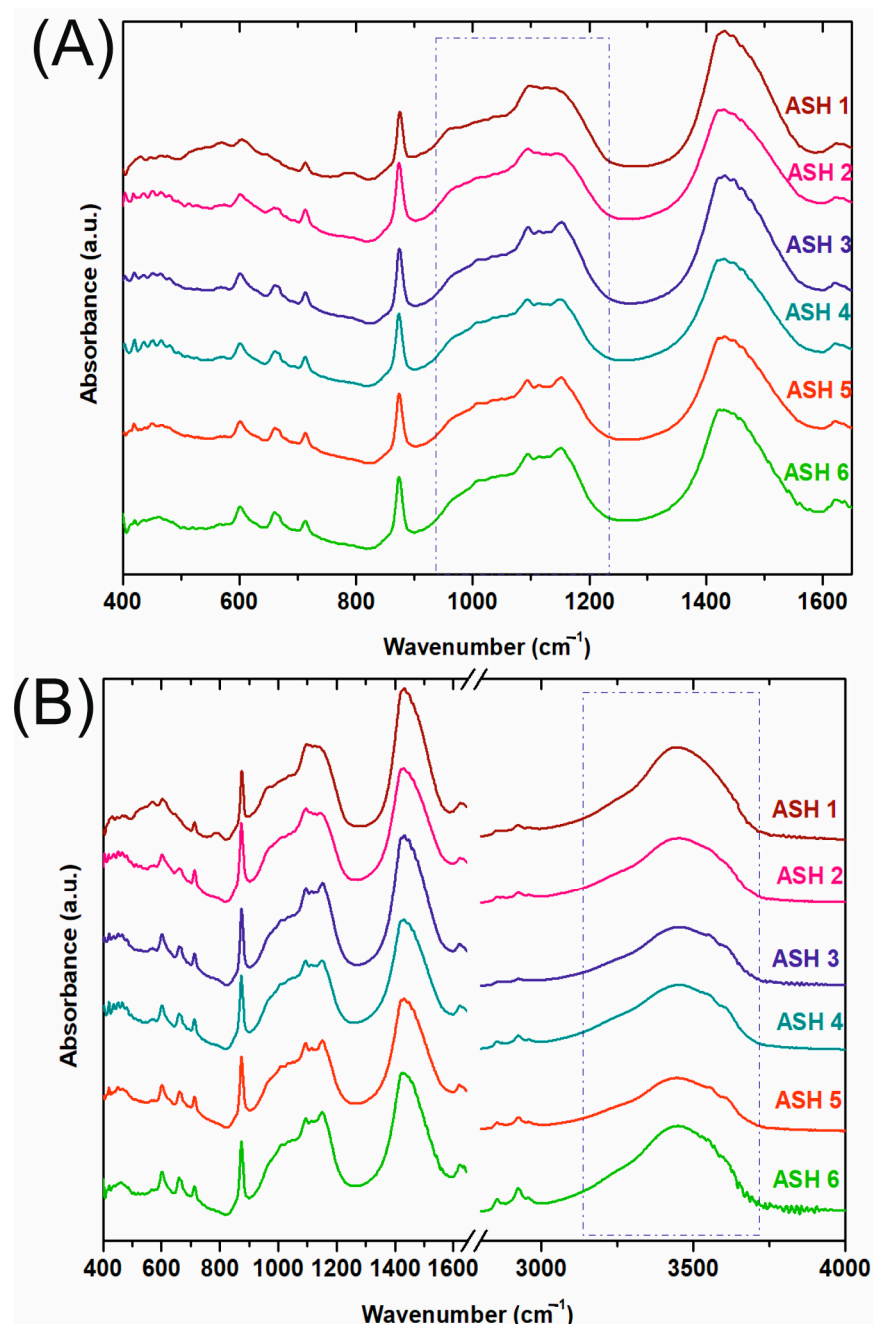


Figure 7. FT-IR spectra of the ASH 1 to ASH 6 samples in the range of (A) 400–1600 cm⁻¹ and (B) 400–4000 cm⁻¹.

3.2.4. UV-Vis Spectra and Gap Energy

Figure 8 presents the UV-Vis spectra of the studied samples. The analysis of the UV-Vis data indicates absorption bands that are specific to electronic transitions due to the presence of transient metal ions, such as iron, in agreement with the XRD data. Fe⁺² ions can indicate t_{2g} → e_g electronic transitions in the range between 750 and 1050 nm. Fe⁺³ ions produce absorption bands in the region between 400 and 550 nm. The intensity of these bands reaches maximum values for ASH 1 and minimum values for ASH 2 [31].

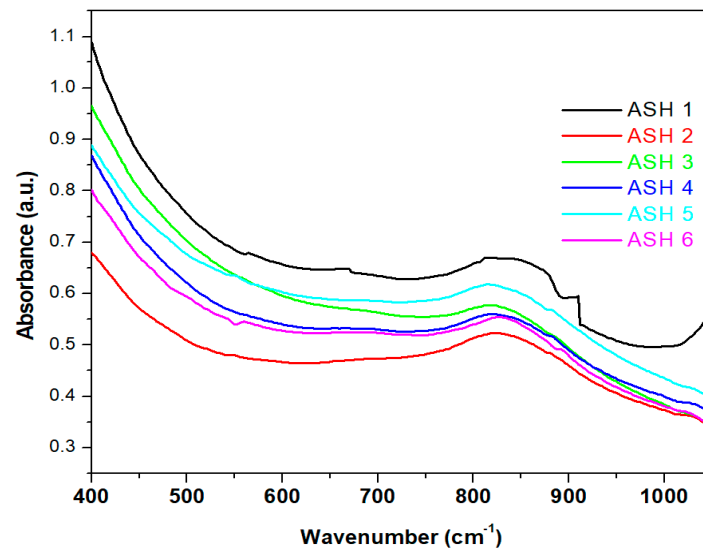


Figure 8. UV-Vis for all of the bottom ash samples.

The values of the optical gap energy, E_g , obtained from the extrapolation of the linear portion of the plot, $(\alpha h\nu)^2$, as a function of $h\nu$, when $\alpha h\nu \rightarrow 0$, for the studied samples are shown in Figure 9. From these dependencies, it can be observed that the compositional evolution of the optical gap energy decreases compared to the ASH 1 sample and reaches the lowest value for the ASH 3 sample. The optical gap energy values are in the range between 2.27 and 2.52 eV, which indicates the semiconducting behavior of the ASH samples. Decreases in the gap energy values can be attributed to lattice defects.

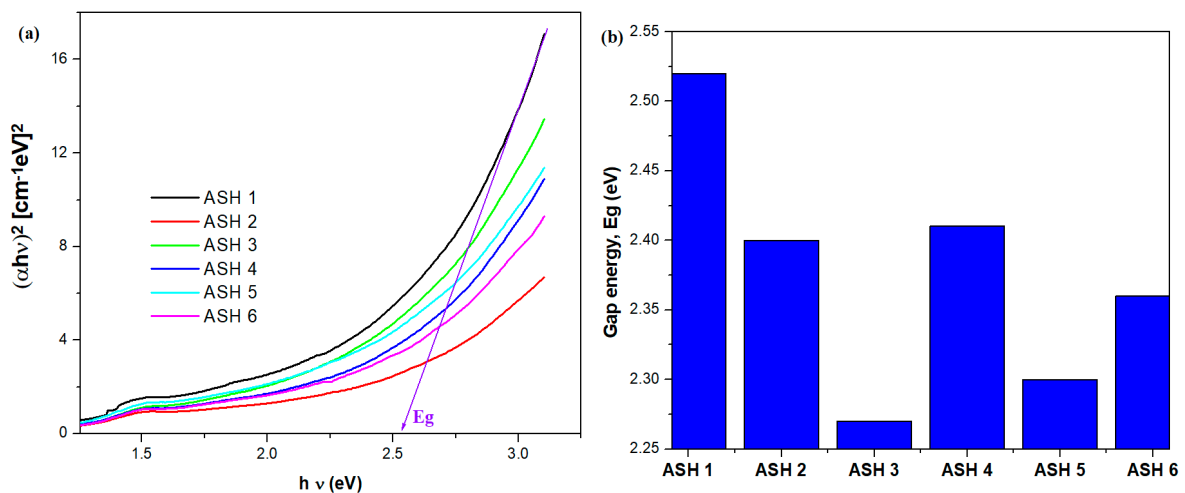


Figure 9. (a) The energy gap that was obtained from the extrapolation of the linear portion, and (b) the energy gap for all of the bottom ash samples.

3.3. Textural Characteristics

3.3.1. N₂ Adsorption–Desorption Isotherms

In Figure 10, the nitrogen adsorption and desorption isotherms that were obtained using the low-pressure method at $-196.15\text{ }^\circ\text{C}$ are shown. The presented curves illustrate the relationship between the relative nitrogen vapor pressure (p/p_0) and the volume of gas adsorbed, expressed as the standard gas volume units, STP ($0\text{ }^\circ\text{C}$ and 1 atm), in the mass of the bottom ash sample. The isotherm range covers relative pressures, p/p_0 , from 0 to 1, with nitrogen condensation occurring in the sample pores at $p/p_0 = 1$. Based on the shape of the obtained isotherms, extensive information about the studied material was

acquired. The identification of the isotherm type allows for an assessment of the adsorption process, whether it is monolayer or multilayer, and the presence of capillary condensation or micropore filling [38].

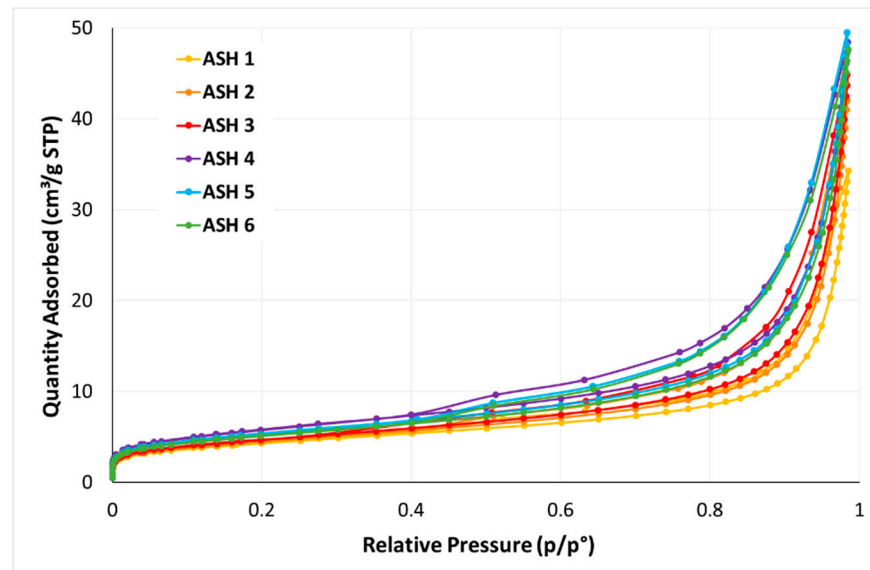


Figure 10. Nitrogen adsorption and desorption isotherms for bottom ash samples at $-196.15\text{ }^{\circ}\text{C}$.

At low relative pressures, an increase in the adsorption isotherm was observed, associated with the filling of micropores with widths that were two or three times the diameter of the molecules. The micropore capacity for nitrogen at $-196.15\text{ }^{\circ}\text{C}$ is indicated by a horizontal plateau, although it is not fully horizontal in the isotherms shown.

The nitrogen adsorption isotherms for the bottom ash samples could be classified as type II isotherms, according to the IUPAC [35], which are characteristic of non-porous or macroporous materials that have a small contribution of micropores and a low internal surface area. Type II isotherms result from the unlimited physical adsorption of gas and are characterized by the multilayer filling of pores. At low p/p_0 values, the shape of the adsorption branch resembles a type I isotherm, indicating that the micropores are filled with gaseous adsorbate, as in the case of methane adsorption on coal [39–41]. For the bottom ash samples, only in the initial range of the isotherm is a monomolecular layer (consisting of N_2 molecules) formed on the surface. As the relative pressure increases, a multilayer is formed, up to high relative nitrogen pressures, p/p_0 . The shape of the type II isotherm was observed for fly ash from a power station [38,42]. According to Tian et al. [23], the mechanism of the adsorption process on bottom ash was found to be monolayer heterogeneous adsorption. The adsorption capacity at low relative pressures (up to p/p_0 around 0.01) indicates the presence of micropores [35]. The occurrence of such features in bottom ash has been previously reported [43].

For all of the seasoned bottom ash samples, a hysteresis loop was observed on the adsorption–desorption isotherms. Determining the type of hysteresis loop is important due to its close relationship with the features of the pore structure and the adsorption mechanism. The nitrogen adsorption isotherms on the bottom ash samples that were obtained show the features of the H3-type hysteresis loop, which can be seen in Figure 10. In the case of H3 hysteresis, the shape of the adsorption branch resembles a type II isotherm, and there is a sharp decrease in the desorption branch in a narrow p/p_0 range, which, for nitrogen, occurred at 77 K, in accordance with Figure 10, i.e., at a relative pressure, p/p_0 , from about 0.4 to 0.5 [35]. The H3 hysteresis loop begins at a relatively low pressure level. This is due to the small content of micropores in the structure of the bottom ash [38]. The presence of H3-type hysteresis applies to materials that are characterized by a slotted mesoporous structure and are associated with capillary condensation occurring between two planes.

The H3 hysteresis loop relates to materials with slit-shaped pores (slit-like pores). It can be noted that the bottom ash samples are characterized by a slit-like mesoporous structure.

According to the curves presented in Figure 10, a slight increase in the mesoporosity content was observed in the samples that were seasoned for a longer period of time, which can be seen in the isotherm graphs as an increase in the area of the hysteresis loop. The mesoporosity of the ASH 4 and ASH 6 samples was richer than that of the other ash samples. ASH 4 and ASH 6 had a larger hysteresis loop area than the other four bottom ashes. Compared to fly ash, the hysteresis loops of the bottom ash samples were narrow and had smaller pore volumes.

3.3.2. Quantity Adsorbed

The textural properties of bottom ash samples, calculated on the basis of the adsorption isotherms presented in Figure 10, are included in Table 3. Although the adsorption and desorption isotherms of six bottom ash samples (Figure 10) had a similar course, the adsorption capacity of the bottom ash subjected to different seasoning periods varied. As it may be seen from Table 3, as the seasoning time increased, an increase in adsorbed quantity was observed, which for the shortest seasoned ash (ASH 1) was the smallest ($34.3 \text{ cm}^3/\text{g}$), while for the ASH 5 sample adsorbed quantity was the largest and amounted to $49.5 \text{ cm}^3/\text{g}$. The ASH 6 sample had a similar adsorption capacity to the ASH 5 sample, comparable to the adsorption capacity of the ASH 4.

Table 3. Textural properties of bottom ash samples.

		ASH 1	ASH 2	ASH 3	ASH 4	ASH 5	ASH 6
Quantity Adsorbed at $p/p_0 = 0.98$	cm^3/g (STP)	34.30	41.98	44.84	48.42	49.49	47.63
Surface Area							
BET Surface Area: S_{BET}	m^2/g	15.2	15.9	16.6	20.5	18.9	18.0
Single Point Surface Area: S_{SBET}	m^2/g	14.8	15.5	16.2	19.9	18.4	17.6
T-Plot Micropore Surface Area:	m^2/g	1.15	1.02	0.93	0.87	1.36	1.27
T-Plot External Surface Area:	m^2/g	14.02	14.87	15.67	19.62	17.50	16.78
BJH Cumulative Surface Area:	m^2/g	15.98	15.86	16.75	20.82	19.07	18.30
Pore Volume							
BJH Cumulative Volume Of Pores: V_p	cm^3/g	0.05215	0.06353	0.06772	0.07334	0.07478	0.07191
T-Plot Micropore Volume: V_{micro}	cm^3/g	0.00054	0.00044	0.00040	0.00034	0.00061	0.00058
V_{meso}	cm^3/g	0.05161	0.06309	0.06732	0.073	0.07417	0.07133
V_{micro} Content	%	1.04	0.69	0.59	0.46	0.82	0.81
V_{meso} Content	%	98.96	99.31	99.41	99.54	99.18	99.19
Pore Size							
Average Pore Width (by BET): d_{av}	nm	12.00	13.96	14.42	13.18	14.54	14.12

3.3.3. Surface Area

The determined specific surface areas, both S_{BET} and S_{SBET} , were small and ranged from about $15 \text{ m}^2/\text{g}$ to over $20 \text{ m}^2/\text{g}$, depending on the sample. As can be seen from Table 3, a longer seasoning time positively influenced the increase in the specific surface area of the bottom ash. The highest specific surface area among the studied samples was observed for ASH 4, which exhibited a 25% higher S_{BET} surface area compared to sample ASH 1. The longest-seasoned samples, ASH 5 and ASH 6, had higher surface areas by 18.0% and 13.7%, respectively, compared to the shortest-seasoned bottom ash sample. According to Chiang et al. [43], the S_{BET} specific surface area for the raw bottom ash was only $4.6 \text{ m}^2/\text{g}$.

The studied ash samples had a relatively large external surface area compared to their internal surface area. The measured micropore surface area values ranged from 0.87 to 1.36 m²/g, with an average value of 1.10 m²/g, depending on the bottom ash sample. Sample ASH 4, with the highest specific surface area, had the lowest micropore surface area, constituting only 4.4% of the total internal surface area of the bottom ash. For the other bottom ash samples, the micropore surface area accounted for 6% to 8% of the specific surface area.

3.3.4. Pore Volume and Size

Figure 11 shows the cumulative pore volume for the studied bottom ash samples, based on the nitrogen adsorption data, plotted against pore width and determined using the BJH theory. The curves in Figure 11 reveal differences in the porosity of the samples. As shown in Table 3, the total pore volume for adsorption in the range of pore sizes 17.62–1092.5 Å (1.7–110 nm) ranged from 0.0020 to 0.0677 cm³/g for ASH 3. The largest pore volume among the tested bottom ash samples, amounting to 0.0748 cm³/g, was found in ASH 5, which was seasoned for more than five months. The smallest pore volume, 0.0522 cm³/g, was observed in the shortest-seasoned sample, ASH 1. Consequently, ASH 6 had a 43% higher total pore volume in the mesopore range than the shortest-seasoned sample, ASH 1.

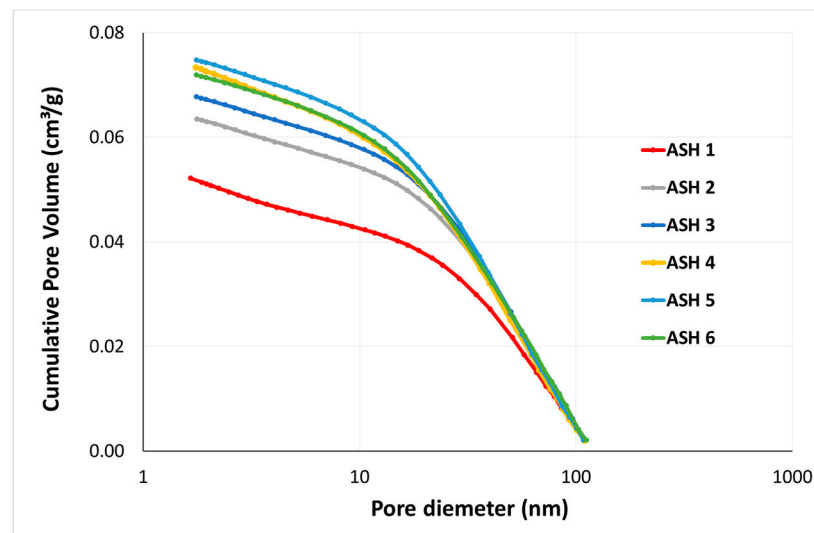


Figure 11. Adsorption cumulative pore volume of bottom ash samples subjected to seasoning (BJH).

Figure 12 presents the dV/dD derivative values on a logarithmic scale. Figure 12 shows the pore volume distribution curves as a function of their diameter for the studied bottom ash samples. In Figure 12, local dominant pore diameters are visible, which were not discernible in the cumulative data from Figure 11. As can be seen from the obtained curves, all of the seasoned samples exhibited a heterogeneous pore volume distribution. A bimodal distribution was noticeable. In Figure 12, two significant pore size maxima are evident: one of these is at the boundary between microporosity and mesoporosity, according to IUPAC, clearly marked at 1.75 nm. This maximum dominates over the second, less distinct one, which shifts from around 30 nm in sample ASH 1 to 17.5 nm in sample ASH 6. The less pronounced maximum is related to both pores and microcracks in the studied material. Observations from Figure 12 can be summarized as, together with longer seasoning time in a closed storage facility, the smaller-amplitude maximum is moving towards smaller pore widths.

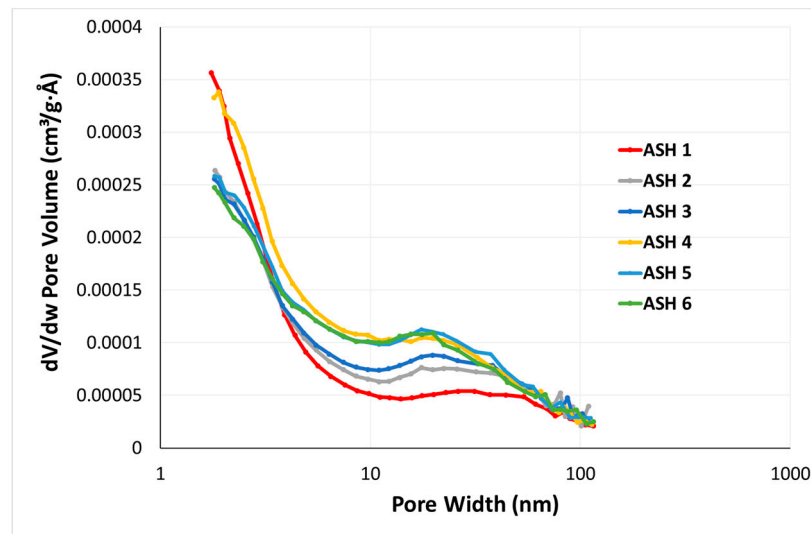


Figure 12. Adsorption dV/dD derivative pore volume in logarithmic scale for the studied bottom ash samples (BJH).

Figure 13 shows the pore volume distribution of mesopores and some macropores in the bottom ash samples. The displayed distribution primarily covered transitional pores (mesopores), larger than the size of the adsorbing molecules. The pore volume distribution did not include the smallest pores (micropores) with sizes below the lower limit of mesopores (<2.0 nm). As can be observed from the displayed graphs, the largest pore volume in the studied samples was for pores with diameters in the range between 20–40 nm and 38–60 nm. A characteristic increase in the maximum amplitude of 30 nm was seen in the longer-seasoned samples, but only up to a certain point, which was the same for ASH 4, ASH 5, and ASH 6. Thus, in the 21st week of seasoning, the growth in pore volume, with diameters ranging from 20 to 40 nm, stabilized. Figure 13 also shows varying maximum amplitudes associated with the presence of microcracks in the bottom ash, indicating the randomness of amplitude occurrence from about 70 nm to 110 nm, regardless of the seasoning duration.

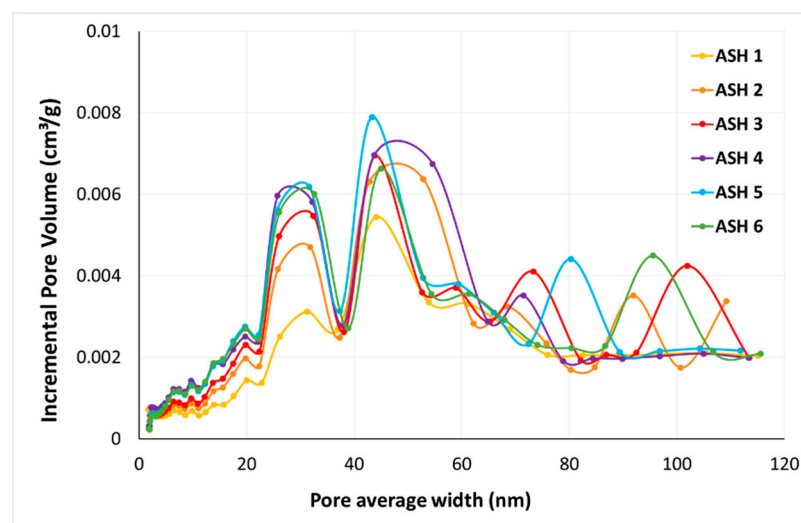


Figure 13. Incremental pore volume distribution as a function of the pore diameter for the bottom ash samples.

Figure 14 presents the pore volume distribution of the studied bottom ash samples. The obtained distribution included a part of the macropores, transitional pores (mesopores),

and the smallest pores (micropores). As it may be observed from the presented curves that the pore area distribution of the seasoned bottom ash was multimodal, with the main peaks seen at around 2.0 nm, 30 nm, and 45 nm and several smaller peaks in the pore diameter range between 60 nm and 120 nm.

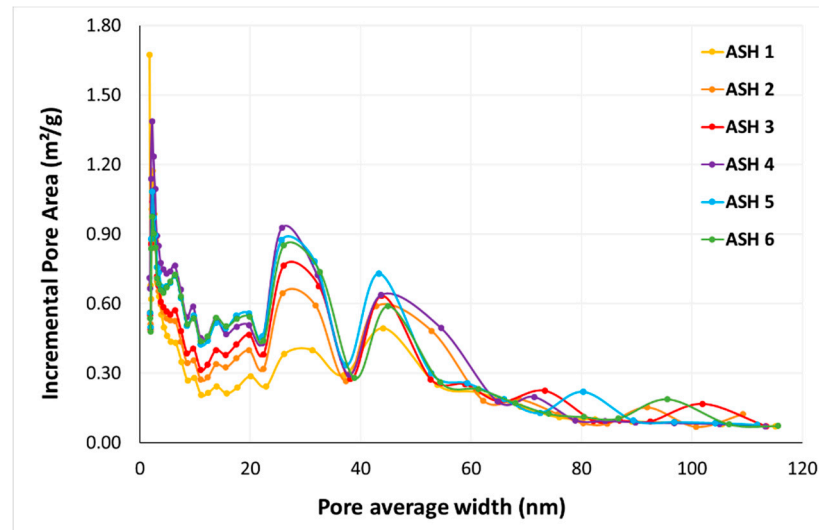


Figure 14. Incremental pore area distribution as a function of the pore diameter for the bottom ash samples.

The peak at 2.0 nm amplitude is at the boundary of the microporosity region and results from the shape of the nitrogen adsorption isotherm at low pressure values. A comparison of the curves from Figure 14 revealed a systematic development of the mesopore surface area in the pore size range from over 2.0 nm to about 50 nm, resulting from the extended seasoning time of the bottom ash in a closed storage facility. The analysis of the pore area distribution within the macropore range revealed maxima with similar amplitudes that were associated with the presence of microcracks in the bottom ash.

The pore size distributions (PSDs) that were determined for the pore diameter range from 1.0 nm to 120 nm were characterized by an average pore width d_{av} , ranging from 12.0 to 14.5 nm, depending on the seasoning time. The average value obtained for all of the bottom ash samples was 13.7 nm.

4. Conclusions

Based on the research conducted, the following conclusions can be drawn:

- The seasoning process contributed to changes in the bottom ash, as detected by the structural analysis methods. It was shown that the seasoning process resulted in the drying of material under closed storage conditions.
- Analyses of ASH 1, ASH 4, and ASH 6 revealed the presence of water and/or hydroxyl units in the samples. Studies of ASH 2, ASH 3, and ASH 5, on the other hand, showed lower hydroxyl or water contents in the samples. The presence of two crystalline phases, SiO_2 and CaCO_3 , in the bottom ash suggests applications in the concrete industry, where CaCO_3 provides long-term mechanical strength to concrete.
- The length of the seasoning process had an impact on the textural parameters of the samples. The seasoning of the material had a beneficial effect on the increase in the specific surface area (25% higher S_{BET} (surface area) compared to the shortest-seasoned bottom ash, ASH 1), external surface area (a 28.5% increase in the case of ASH 4), and microporosity (13% increase).
- The seasoning process positively affected the textural parameters of the bottom ash, such as the transformation of a part of the mesopore area in favor of smaller pores, related to the moving of the maximum pore volume amplitude towards smaller pores.

In the 21st week of seasoning, the growth of the pore volume in the pore size range from 20 to 40 nm stabilized.

- Studies on the bottom ash that was seasoned for 31 weeks showed that waste from an incineration plant could be used not only for road construction purposes but also in the concrete industry and for environmental purposes, which would enable its wider utilization and recycling. The oxide composition and textural features indicate the potential for modifying the surface of bottom ash to obtain a more developed texture that is similar to that of zeolites.

Author Contributions: Conceptualization, B.D., K.G. and S.R.; methodology, B.D., S.R., K.G., D.M. and R.I.C.; software, M.T., B.D. and S.R.; validation, B.D. and K.G.; formal analysis, B.D.; investigation, B.D., S.R., D.M., R.I.C. and M.T.; resources, B.D. and K.G.; data curation B.D. and M.T.; writing—original draft preparation, B.D.; writing—review and editing, B.D., D.M., R.I.C. and K.G.; visualization, K.G. and M.T.; supervision, B.D.; project administration, B.D. and K.G.; funding acquisition, K.G. All authors have read and agreed to the published version of the manuscript.

Funding: This work was prepared as a part of the joint Polish–Romanian project Macro and micro strength tests on composite—cement stones under the agreement on scientific cooperation between the Polish Academy of Sciences and the Romanian Academy.

Institutional Review Board Statement: Not applicable.

Informed Consent Statement: Not applicable.

Data Availability Statement: All data used to create the article are available from the authors.

Acknowledgments: The authors would like to thank Radu Fechet for the useful discussion related to the NMR method. The authors would like to thank Krakowski Holding Komunalny S.A. Thermal Waste Processing Plant in Krakow for providing the research material and necessary information regarding the waste generated.

Conflicts of Interest: The authors declare no conflict of interest.

References

1. Olejnik, D.; Krupa, M. Selected thermal was treatment plants in Europe, case study. *Civ. Environ. Eng. Rep. CEER* **2023**, *33*, 0001–0018. [CrossRef]
2. Wielgosinski, G. Termiczne Przekształcanie Odpadów. Wydawnictwo Nowa Energia. 2020. Available online: <https://nowaenergia.com.pl/wydawnictwa-ksiazkowe/> (accessed on 23 October 2022).
3. Rosik-Dulewska, C. *Podstawy Gospodarki Odpadami; Środowisko; Wydawnictwo Naukowe PWN: Stryków, Poland, 2023; pp. 10–250. (In Polish)*
4. Available online: <https://khk.krakow.pl/pl/ekospalarnia/> (accessed on 30 October 2024).
5. Rozporządzenie Ministra Klimatu z dnia 2 stycznia 2020 r. w sprawie katalogu odpadów (In Polish). Available online: <https://isap.sejm.gov.pl> (accessed on 10 June 2024).
6. Wang, J.; Feng, Y.; He, Y. Advancements in recycling technologies for waste CIGS photovoltaic modules. *Nano Energy* **2024**, *128 Pt A*, 109847. [CrossRef]
7. Bayuseno, A.P.; Schmahl, W.W. Understanding the chemical and mineralogical properties of the inorganic portion of MSWI bottom ash. *Waste Manag.* **2010**, *30*, 1509–1520. [CrossRef] [PubMed]
8. Su, L.; Wu, S.; Zhu, W.; Liang, B.; Zhang, X.; Yang, J. Enhanced geopolymerization of MSWI fly ash through combined activator pretreatment: A sustainable approach to heavy metal encapsulation and resource recovery. *J. Environ. Manag.* **2024**, *370*, 122870. [CrossRef]
9. Murray, A.; Skene, K.; Haynes, K. The Circular Economy: An Interdisciplinary Exploration of the Concept and Application in a Global Context. *J. Bus. Ethics* **2017**, *140*, 369–380. [CrossRef]
10. Tang, P. Municipal Solid Waste Incineration (MSWI) Bottom Ash—From Waste to Value: Characterization, Treatments and Application. Ph.D. Thesis, Technische Universiteit Eindhoven, Eindhoven, The Netherlands, 2017.
11. del Valle-Zermeño, R.; Formosa, J.; Chimenos, J.M.; Martínez, M.; Fernández, A.I. Aggregate Material Formulated with MSWI bottom Ash and APC Fly ash for Use as Secondary Building Material. *Waste Manag.* **2013**, *33*, 621–627. [CrossRef]
12. Cho, B.H.; Nam, B.H.; An, J.; Youn, H. Municipal Solid Waste Incineration (MSWI) Ashes as Construction Materials—A Review. *Materials* **2020**, *13*, 3143. [CrossRef] [PubMed]
13. Aubert, J.E.; Husson, B.; Sarramone, N. Utilization of municipal solid waste incineration (MSWI) fly ash in blended cement. *J. Hazard. Mater.* **2007**, *146*, 12–19. [CrossRef]

14. Qiao, X.C.; Tyrer, M.; Poon, C.S.; Cheeseman, C.R. Novel cementitious materials produced from incinerator bottom ash. *Resour. Conserv. Recycl.* **2008**, *52*, 496–510. [[CrossRef](#)]
15. Wang, L.; Jin, Y.; Nie, Y.; Li, R. Recycling of municipal solid waste incineration fly ash for ordinary Portland cement production: A real-scale test. *Resour. Conserv. Recycl.* **2010**, *54*, 1428–1435. [[CrossRef](#)]
16. Kim, J.; An, J.; Nam, B.H.; Tasneem, K.M. Investigation on the side effects of municipal solid waste incineration ashes when used as mineral addition in cement-based material. *Road Mater. Pavement Des.* **2015**, *17*, 345–364. [[CrossRef](#)]
17. Yang, Z.; Ji, R.; Liu, L.; Wang, X.; Zhang, Z. Recycling of municipal solid waste incineration by-product for cement composites preparation. *Constr. Build. Mater.* **2018**, *162*, 794–801. [[CrossRef](#)]
18. Czuma, N.; Casanova, I.; Baran, P.; Szczurowski, J.; Zarebska, K. CO₂ sorption and regeneration properties of fly ash zeolites synthesized with the use of differentiated methods. *Sci. Rep.* **2020**, *10*, 1825. [[CrossRef](#)] [[PubMed](#)]
19. Franus, W. Materiał zeolitowy typu X otrzymany z popiołu lotnego w wyniku syntezy hydrotermalnej i niskotemperaturowej. *Bud. I Architekt.* **2010**, *7*, 25–34. (In Polish) [[CrossRef](#)]
20. Ashraf, M.S.; Ghoul, Z.; Shao, Y. Production of eco-cement exclusively from municipal solid waste incineration residues. *Resour. Conserv. Recycl.* **2019**, *149*, 332–342. [[CrossRef](#)]
21. Chuang, C.-W.; Chen, T.-A.; Huang, R. Effect of Finely Ground Coal Bottom Ash as Replacement for Portland Cement on the Properties of Ordinary Concrete. *Appl. Sci.* **2023**, *13*, 13212. [[CrossRef](#)]
22. Chindasiriphan, P.; Meenyut, B.; Orasutthikul, S.; Jongvivatsakul, P.; Tangchirapat, W. Influences of high-volume coal bottom ash as cement and fine aggregate replacements on strength and heat evolution of eco-friendly high-strength concrete. *J. Build. Eng.* **2023**, *65*, 105791. [[CrossRef](#)]
23. Tian, A.; Zhou, Y.; Chen, Y.; Kan, D.; Lu, Y.; Tang, Q. Use of municipal solid waste incineration (MSWI) bottom ash as a permeable subgrade material: An experimental and mechanism study. *J. Air Waste Manag. Assoc.* **2024**, *74*, 291–303. [[CrossRef](#)]
24. Czuma, N.; Zarebska, K.; Baran, P.; Gauden, P. The use of mathematical models for modelling sulphur dioxide sorption on materials produced from fly ashes. *Energetika* **2018**, *64*, 105–112. [[CrossRef](#)]
25. Parzenty, H.R.; Róg, L. Initial assessment of variability in the modes of occurrence of some trace elements in coal seams with vertical profiles in the Upper Silesian Coal Basin in Poland. *Arch. Min. Sci.* **2020**, *65*, 723–736. [[CrossRef](#)]
26. Fehete, R.; Demco, D.E.; Zhu, X.; Tillmann, W.; Möller, M. Water States and Dynamics in Perfluorinated Ionomer Membranes by ¹H One- and Two-Dimensional NMR Spectroscopy, Relaxometry, and Diffusometry. *Chem. Phys. Lett.* **2014**, *597*, 6–15. [[CrossRef](#)]
27. Fehete, R.; Demco, D.E.; Blümich, B. Enhanced sensitivity to residual dipolar couplings by high-order multiple-quantum NMR. *J. Magn. Reson.* **2004**, *169*, 19–26. [[CrossRef](#)] [[PubMed](#)]
28. Moldovan, D.; Fehete, R. Bimodal ¹H double quantum build-up curves by Fourier and Laplace-like transforms on aged cross-linked natural rubber. *Polymers* **2021**, *13*, 3523. [[CrossRef](#)] [[PubMed](#)]
29. Rondeau-Mouro, C.; Kovrljija, R.; Van Steenberge, E.; Moussaoui, S. Two dimensional IR-FID-CPMG acquisition and adaptation of a maximum entropy reconstruction. *J. Magn. Reson.* **2016**, *265*, 16–24. [[CrossRef](#)] [[PubMed](#)]
30. Wang, H.; Tian, L.; Zhang, K.; Liu, Z.; Huang, C.; Jiang, L.; Chai, X. How Is Ultrasonic-Assisted CO₂ EOR to Unlock Oils from Unconventional Reservoirs? *Sustainability* **2021**, *13*, 10010. [[CrossRef](#)]
31. Rada, R.; Manea, D.L.; Chelcea, R.; Rada, S. Nanocomposites as Substituent of Cement: Structure and Mechanical Properties. *Materials* **2023**, *16*, 2398. [[CrossRef](#)]
32. Chelcea, R.I.; Danis, D.; Fehete, R. Structural and Kinetic Characterization of Unexpired and Expired Drugs by Proton Nuclear Magnetic Resonance (¹H NMR) Relaxometry and Fourier Transform Infrared (FT-IR) Spectroscopy. *Anal. Lett.* **2022**, *56*, 372–389. [[CrossRef](#)]
33. Brunauer, S.; Emmett, P.H.; Teller, E. Adsorption of gases in multimolecular layers. *J. Am. Chem. Soc.* **1938**, *60*, 309–319. [[CrossRef](#)]
34. Livingston, H. The cross-sectional areas of molecules adsorbed on solid surfaces. *J. Colloid Sci.* **1949**, *4*, 447–458. [[CrossRef](#)]
35. Thommes, M.; Kaneko, K.; Neimark, A.V.; Olivier, J.P.; Rodriguez-Reinoso, F.; Rouquerol, J.; Sing, K.S.W. Physisorption of gases, with special reference to the evaluation of surface area and pore size distribution (IUPAC Technical Report). *Pure Appl. Chem.* **2015**, *87*, 1051–1069. [[CrossRef](#)]
36. Proksa, J.; Łączny, M.J.; Bzowski, Z. Evaluation of the possibility of using granulated carbonated volatile fly ash from fluidized beds (G-CVFA) in underground mining techniques. *Arch. Min. Sci.* **2020**, *65*, 737–750. [[CrossRef](#)]
37. Godyń, K.; Dutka, B.; Tram, M. Application of Petrographic and Stereological Analyses to Describe the Pore Space of Rocks as a Standard for the Characterization of Pores in Slags and Ashes Generated after the Combustion of Municipal Waste. *Materials* **2023**, *16*, 7706. [[CrossRef](#)] [[PubMed](#)]
38. Majchrzak-Kuceba, I.; Nowak, W. A thermogravimetric study of the adsorption of CO₂ on zeolites synthesized from fly ash. *Thermochim. Acta* **2005**, *437*, 67–74. [[CrossRef](#)]
39. Dutka, B.; Godyń, K. Predicting variability of methane pressure with depth of coal seam. *Przemysł Chem.* **2018**, *97*, 1344–1348. [[CrossRef](#)]
40. Qi, L.; Tang, X.; Wang, Z.; Peng, X. Pore characterization of different types of coal from coal and gas outburst disaster sites using low temperature nitrogen adsorption approach. *Int. J. Min. Sci. Technol.* **2017**, *27*, 371–377. [[CrossRef](#)]
41. Nie, B.; Liu, X.; Yang, L.; Meng, J.; Li, X. Pore structure characterization of different rank coals using gas adsorption and scanning electron microscopy. *Fuel* **2015**, *158*, 908–917. [[CrossRef](#)]

42. Ściubidło, A.; Majchrzak-Kuceba, I. Exhaust gas purification process using fly ash-based sorbents. *Fuel* **2019**, *258*, 116126. [[CrossRef](#)]
43. Chiang, Y.W.; Ghyselbrecht, K.; Santos, R.M.; Meesschaert, B.M.; Martens, J.A. Synthesis of zeolitic-type adsorbent material from municipal solid waste incinerator bottom ash and its application in heavy metal adsorption. *Catal. Today* **2012**, *190*, 23–30. [[CrossRef](#)]

Disclaimer/Publisher’s Note: The statements, opinions and data contained in all publications are solely those of the individual author(s) and contributor(s) and not of MDPI and/or the editor(s). MDPI and/or the editor(s) disclaim responsibility for any injury to people or property resulting from any ideas, methods, instructions or products referred to in the content.